1-28-2015

A High Resolution Study of the Magnetic Fields in the Centaurus Cluster

Caleb Grimes

Caleb Grimes
Candidate

Physics and Astronomy
Department

This thesis is approved, and it is acceptable in quality and form for publication:

Approved by the Thesis Committee:

Dr. Gregory Taylor , Chairperson

Dr. Richard Rand

Dr. Ylva Pihlstrom

A High Resolution Study of the Magnetic Fields in the Centaurus Cluster

by

Caleb K. Grimes

B.S., Physics, Morehead State University, 2012

THESIS

Submitted in Partial Fulfillment of the

Requirements for the Degree of

Master of Science

Physics

The University of New Mexico

Albuquerque, New Mexico

December, 2014

Dedication

I dedicate this to my parents, Greg and Kathleen Grimes, who have always been of immense support throughout my education and without which I could not have succeeded.

Acknowledgments

I would like to acknowledge my advisor, Dr. Greg Taylor, my defense committee Dr. Taylor, Dr. Rand, and Dr. Pihlstrom and all of my collaborators on this project.

I also would like to acknowledge the support provided by the National Aeronautics and Space Administration through Chandra Award Numbers G01-12156X, GO2-13149X and GO4-15121X issued by the Chandra X-ray Observatory Center, which is operated by the Smithsonian Astrophysical Observatory for and on behalf of the National Aeronautics Space Administration under contract NAS8-03060

A High Resolution Study of the Magnetic Fields in the Centaurus Cluster

by

Caleb K. Grimes

B.S., Physics, Morehead State University, 2012

M.S., Physics, University of New Mexico, 2014

Abstract

Galaxy clusters are of particular interest to astronomers because they provide test beds for probing the Cosmic Web which they occupy. Probing nearby galaxy clusters, such as the Centaurus Cluster, can lead to further insight into the understanding of interactions and evolution within galaxy clusters. We seek to take advantage of the Very Large Array's (VLA) high angular and spatial resolution to determine the polarimetry characteristics of the radio source at the center of the Centaurus Cluster: PKS1246-410. We have obtained total intensity maps, as well as, the highest resolution Rotation Measure (RM) map of PKS1246-410 to date. We have found four regions of enhanced RMs that deviate 3σ from the mean distribution of RMs. Using these RMs we estimate the magnetic field in the Centaurus cluster to be $5.4\mu G$ and $3.23\mu G$ for an uniform and tangled magnetic field model, respectively. We discuss the implications of these results on our understanding of ICM magnetic fields.

Contents

List of Figures

List of Figures

List of Tables

Glossary

VLA: the Very Large Array is an array of 27, 25 meter radio antennas located near Socorro, NM. The VLA is sometimes also referred to as the Expanded VLA or Jansky VLA

VLBA: the Very Long Baseline Array is an array of 10 radio antennas, each with a dish 25 meters in diameter, which span over more than 5,000 miles.

Chandra: a X-ray satellite in a highly elliptical orbit which it completes in 64 hours. Chandra was formerly known as Advanced X-ray Astrophysics Facility (AXAF).

CASA: Common Astronomy Software Application is a data reduction software developed by NRAO to be the primary software for VLA and ALMA data.

AIPS: Astronomical Image Processing System is a Fortran based data reduction software. AIPS was the primary software for VLA reduction prior to the implementation of CASA.

DIFMAP: a difference mapping software originally developed for imaging Very Long Baseline Array (VLBA) data.

Glossary

RM: Rotation Measure in units of radians per m^2 created by Faraday Rotation of a polarized wave-front.

ICM: Intracluster Medium. Diffuse gas present within galaxy cluster.

RMCUB: RMCUB is a custom code in AIPS that allows the user to extract the individual RM fits and plots them by Right Ascension and Declination.

Chapter 1

Introduction

1.1 Large Scale Structure of the Universe

The large scale mass distribution in the universe today is the result of the initial conditions during the first moments after the big bang. The mass distribution forms a "web-like" network of filaments, separated by vast voids of space, which we call the Cosmic Web. These filaments contain the vast majority of the baryonic matter in the universe. The intersection points of these filaments result in interaction of a large number of galaxies. As a result of these interactions overtime galaxies coalesce to form groups of galaxies containing 3 to 50 gravitationally bound galaxies on size scales of $\sim$2 Mpc. Given enough time these objects evolve hierarchically to form galaxy cluster containing 50 to 1000 gravitationally bound galaxies on size scales of 10s Mpc. The remaining filamentary structure in the cosmic web is divided into super-clusters which contain multiple gravitationally unbound galaxy clusters. To understand the interactions present in the Cosmic Web we must understand how these galaxies interact and coalesce to form larger scale objects (Feretti et al. 2012).

1.2 Galaxy Clusters

Much of our understanding of the Universe and its history rely on how well we understand the evolution of galaxy clusters. Galaxy clusters are a subject of ongoing interest in the astronomical community due to the fact that they are the largest systems of bound baryonic matter that we can observe. As such, they provide a test bed for understanding the history and evolution of the Cosmic Web. Our current understanding of galaxy clusters suggests that they initially form in smaller groups and then through gravitational attraction merge, ultimately creating the large galaxy clusters containing $\sim 10^{15}$ M_{sun} we see today (Feretti et al. 2012). The larger merger events, known as 'major mergers', can be some of the most energetic events observed (Sarazin C.L. 2002). When these large galaxy clusters undergo major mergers the gas between the galaxies of the cluster, called intracluster medium (ICM), experiences shocks that cause turbulence. This interaction forms temperature gradients, as well as, sub-structure within the ICM. As time progresses these clusters relax by coming into hydrostatic equilibrium and generally settle around a giant galaxy located at the center of the cluster (Feretti et al. 2012). Recent studies have utilized these advancements at the VLA to understand the central kpc of galaxy clusters in an effort to further our understanding of this extremely energetic and seemingly turbulent environment (e.g. PKS0745-191 Cluster: Sanders et al. 2014).

1.3 Open Topics concerning Galaxy Clusters

An ongoing topic of debate and study regarding galaxy clusters continues to be the presence of magnetic fields in the ICM. The formation, evolution and even existence of extended large scale magnetic fields interacting with the ICM is not well understood.

Support for the idea that clusters possess extended magnetic field within the plasma of the ICM comes from the presences of dissociated steep spectrum radio sources and abnormally high rotation measures (RMs). Many astronomers argue that the presences of dissociated steep spectrum radio structures are evidence of a large scale magnetic field interacting with the ICM. This theory suggest that the spectrum from synchrotron emitting plasma steepens as the emitting particles loose energy over time due to confinement by a magnetic field (Section 1.4.2). Very high RMs can also lend credence to the idea that the host cluster possess a magnetic field since the coherence scales of RMs should be much less than the observed kpc variations for an Internal-Faraday screen created by source magnetic field (Section 1.4.1). Other explanations attribute the high rotation measures to thermal mixing with the radio plasma or from thin skins of warm ionized gas in pressure balance with the hot cluster atmospheres as argued in the case of the Centaurus Cluster by Rundnick & Blundell (2003).
To further investigate this rich topic this paper will focus on one of the nearest galaxy clusters, the Centaurus Cluster, located at a distance of only 45Mpc (z=0.0104). We will seek to further our knowledge of the Centaurus cluster by probing the ICM and its interactions with possible magnetic fields present in the environment. Centaurus was specifically chosen as a test bed for probing the ICM due to its proximity and the fact it has a central elliptical galaxy, NGC4696, with an associated polarized radio source PKS1246-410. Throughout this paper we will discuss the highest angular and spatial resolution rotation measure study of PKS1246-410 obtained to date. Using these RM measurement we present estimates for the cluster magnetic field and compare our results with estimates of other similar clusters.

1.4 Cool-Core Clusters

Historically, galaxy clusters have been divided into two classes, based on the X-ray properties at the center of the cluster, called 'cooling-flow' and 'non-cooling-flow' clusters. Cooling-flow clusters are considered to be in a relaxed state (no longer undergoing mergers) and are characterized by a large centrally located galaxy coincident with peaked X-ray emission, indicating high densities. As a result of these high densities, the cooling time required for the hot ICM in the central 100kpc is much less than the Hubble time. Therefore another source of pressure is required to maintain hydrostatic equilibrium or an inward flow of gas will be observed (Fabian, Nulsen & Canizares 1991 , Fabian 1994).

The cooling-flow model suggests that the ICM at the center of the cluster cool and compress due to the pressure of the surrounding gas, during which hot gas from the outer regions flows inward. Evidence from Hα, UV and CO emission seem to contradict this model due to the lack of star formation and molecular gas found in cooling-flow regions (McNamara & O'Connell 1989, Edge 2001). However, the cooling-flow model assumes there is no internal method for heating the gas. Recent studies have sought to address this problem by determining possible mechanisms for heating the gas, such as: conduction, central AGN heating via direct cosmic ray - ICM interactions + conduction, AGN heating by bubble induced weak shocks, soundwave + conduction, and turbulence + conduction (Hudson et al. 2010).

As a result of the cooling-flow model failure to explain multi-wavelength studies a new terminology has been adopted to explain such sources: Cool-Core Clusters (Molendi & Pizzolato 2001). It is generally accepted that cool-core clusters are currently not undergoing mergers and thus considered relaxed, while non-cool-core clusters are currently not in hydrostatic equilibrium due to recent merger events. This definition can lead to difficulty quantifying the actually boundary between cool-core clusters and non-cool-core clusters. A study by Hudson et al. (2010) found it best to defined

this boundary by the central cooling time,t_{cool}, for low redshift clusters. Hudson et al. 2010 defined a cool-core cluster to have a cooling time of $t_{cool} < 7.7h_{71}^{-1/2}$ Gyrs, where $h_{71} \equiv 71$ km s^{-1}Mpc^{-1}.

Over the past decade many cool-core clusters have been the subject of high rotation measure (RM) studies: Cygnus A, Hydra A, Centaurus Cluster, etc. Nearby z$\lesssim$ 0.1 galaxy clusters present a even greater opportunity to study the ICM using high resolution instruments (e.g. VLA and Chandra) down to the central kilo-parsec of the clusters.

Detection of certain radio structures and properties in dense centers of cool-core clusters can aid in the understanding of the dynamics present in the ICM environment; Such structures and properties include radio halos/mini-halos, radio relics and high RMs. In some cases understanding the morphology of halos , mini-halos and relics due to the brightness fluctuation and polarization properties have helped to put constraints on the magnetic field power spectrum, as in the cases of A2255 and A665 (Govoni, Murgia, Feretti 2006 and Vacca, Murgia, Govoni 2010, respectively). In the next section we will briefly discuss the physics behind these structures and expand upon what insights they might give us about the dynamics within cool-core clusters.

1.5 Radio Emission Physics

1.5.1 Faraday Rotation

Faraday Rotation is a phenomenon in which an ionized plasma in the presence of a magnetic field causes linearly polarized light from a background source to experience a differential delay. This delay is seen as a phase shift between the left and right circularly polarized waves creating a rotation of the initial polarization angle ψ_0

intrinsic to the source:

$$\Delta\psi = \psi - \psi_0 = \lambda^2 RM \tag{1.1}$$

where $\Delta\psi$ is the difference in polarization angle, ψ is the observed polarization angle, λ is the wavelength and RM is the Faraday rotation measure. The Faraday rotation measure can then be defined by:

$$RM = 812 \int_0^L n_e B_z dl \quad [\mathrm{rad/m^2}] \tag{1.2}$$

where n_e is the thermal electron density in cm^{-3}, B_z is the magnetic field along the line of sight in μG, and L is the path length through the plasma in kpc (Burn 1966). Using this property we can probe the ICM given we have a polarized source of radiation propagating through the medium. By a linear fit of the λ^2-law in Equation 1.1 we can determine the RM along the line of sight. In the simplest uniform case this RM can then be used in Equation 1.2 to determine the line-of-sight magnetic field of a cluster given the thermal electron distribution which can be found from modeling X-ray emission.

Many studies have determined RMs across extended clusters and found a Gaussian distribution ranging from 100s to 1000s of $\mathrm{rad/m^2}$ (Feretti et al. 2012). These observations indicate that the cluster magnetic field could be turbulent on scales of kpc to 100 pc sizes. One interpretation of these observations is that the intracluster magnetic field is composed of uniform "cells" with a random orientation relative to the observer. In this model the variance is given by:

$$\sigma^2_{RM} = 812 \Lambda_C \int_0^L (n_e B_z)^2 dl \quad [\mathrm{rad^2/m^4}] \tag{1.3}$$

where the RM distribution is assumed to be Gaussian with a mean value of zero and Λ_C is the cell size (Feretti et al. 2012).

Modeling the X-ray emission with a β profile we can further constrain such values as the electron density, core radius and a fitting parameter β (Carrilli & Taylor

2002). Applying these parameters to Equation 1.3 we can derive a more detailed RM dispersion relation for the tangled magnetic field model:

$$\sigma_{RM} = \frac{KBn_e r_c^{1/2} \Lambda_C^{1/2}}{(1 + r^2/r_c^2)^{(6\beta-1)/4}} \sqrt{\frac{\Gamma(3\beta - 0.5)}{\Gamma(3\beta)}} \tag{1.4}$$

where n_e, r_c and β are parameters found through electron density profile (β profile) by X-ray observations, Λ_C is the cell size, r is the distance of the radio source from the center of the cluster, Γ is the Gamma function, K is a factor that depends on the location of the radio source along the line of sight and B is the magnetic field strength (Taylor et al. 2002). Commonly assumed values are K=624 for a source behind the cluster, K=441 if the source is halfway through the cluster and B=$\sqrt{3}B_{||}$, where $B_{||}$ is the parallel component of the magnetic field and in the z-direction.

1.5.2 Spectral Index Studies

Another very useful technique in discerning whether a cluster has a magnetic field is to search diffuse sources with steep spectra from old synchrotron emitting electrons. Synchrotron radiation occurs when a plasma is in the presence of a magnetic field. As the free electrons accelerate around the magnetic field they emit a frequency dependent radiation following a power law: $S_\nu \ \alpha \ \nu^\alpha$, where $\alpha = -0.7$ to -0.8 for synchrotron radiation. As time progresses radio emitting particles lose energy which changes the particle energy distribution. As a result of this energy loss the spectrum steepens due to a cutoff for frequency above the critical frequency, which is dependent on the particle lifetime (Feretti et al. 2012). Therefore we expect for older synchrotron emitting radio sources, such as those at the center of cool-core clusters, to have a steeper spectra than $\alpha = -0.8$.

Diffuse structures not associated with the radio source in galaxy clusters generally are grouped into halos, mini-halos and relics. These classes depend on the location in the cluster and the cluster type (cool-core vs non-cool-core). Halos are located at

center of clusters undergoing mergers (i.e. Non-cool-core clusters). Relics have been detected on the outskirts of both merging and non-merging clusters. Both halos and relics have been discovered in the well studied Coma Cluster (Ferrari et al. 2008). Aside from location, halos and relics have differing polarization amounts such that relics tend to be much more polarized than centrally located halos. The final class of sources, mini-halos, are only detected in the center of cool-core clusters, usually around a powerful radio galaxy (e.g. Perseus Cluster).

All three diffuse source classes have very steep radio spectra which can be measured using spectral index maps. Spectral index studies create total intensity, Stokes I, maps at two frequencies separated by some arbitrary bandwidth. The ratio in flux across the bandwidth can be fit with a power law:

$$S_\nu \ \alpha \ \nu^\alpha \rightarrow \frac{S_{\nu_1}}{S_{\nu_2}} = \left(\frac{\nu_1}{\nu_2}\right)^\alpha; \qquad \therefore \alpha = \frac{ln(S_{\nu_1}) - ln(S_{\nu_2})}{ln(\nu_1) - ln(\nu_2)} \tag{1.5}$$

Such tasks as COMB in AIPS, discussed in Section 2.2, will calculate Equation 1.5 on a pixel by pixel basis. Through this process we can identify steep spectrum sources such as halos, relics and mini-halos to determine the presence and strength of a cluster magnetic field.

1.6 Centaurus Cluster

One source that provides a good test bed for understanding the inner dynamics of galaxy clusters is the Centaurus Cluster (Abell 3526). Centaurus is one of the nearest cool-core clusters (z=0.0104, distance 45Mpc) containing a low power extended radio source ($1.5x10^{24}W\ Hz^{-1}$ at 1.6GHz) coincident with a elliptical galaxy, NGC4696, at the cluster center (Taylor et al. 2002). This radio source, PKS1246-410, has a fortunate property that the emission throughout the galaxy exhibits percent polarization values ranging from 4% to 40% seen in Figure 1.1, excluding regions of missing polarization intensity which we will discuss further in Section 3 and 4. Calculating

the Faraday Rotation (discussed in Section 1.5.1) on the emission from the interior radio galaxy, we can probe the intervening magnetic field required to produce the measured rotation. Utilizing aforementioned techniques combined with the recent improvements to the VLA bandwidth we present the highest spatial and angular resolution RM study of PKS1246-410 to date.

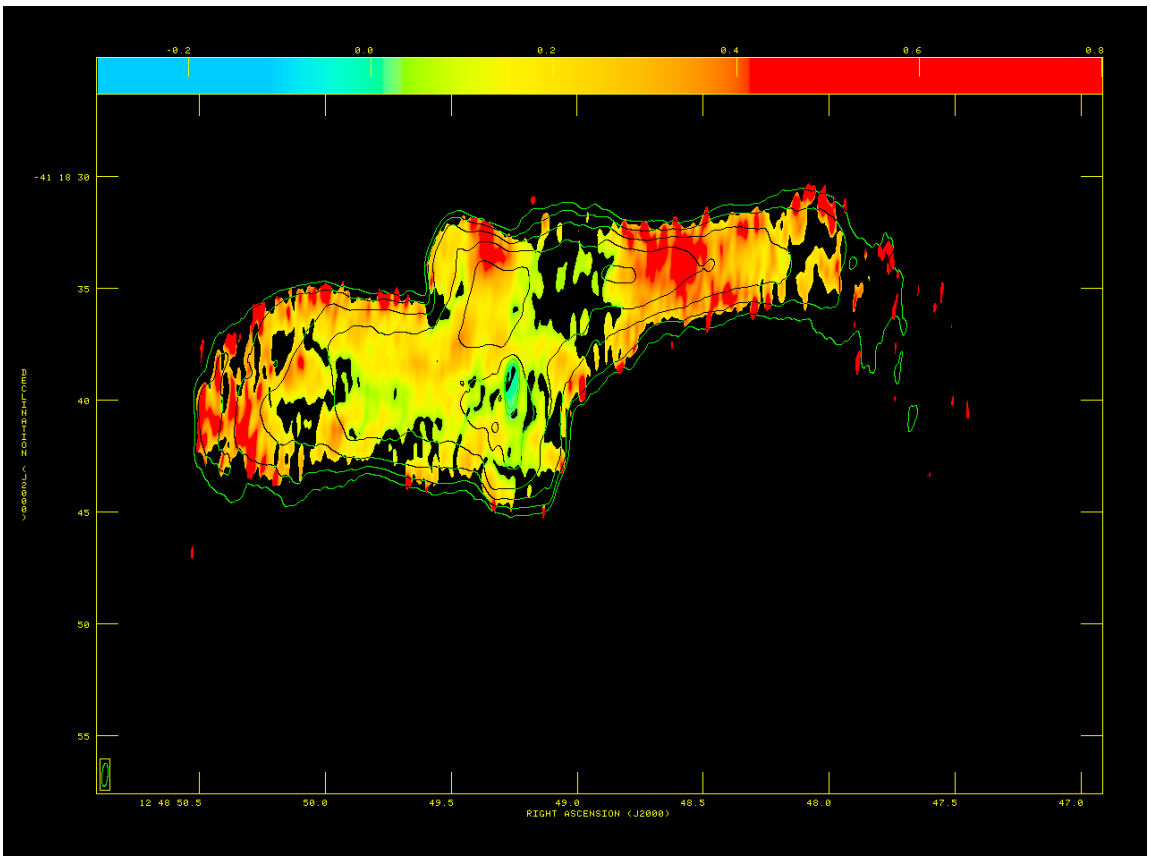

Figure 1.1: Percent polarization for PKS1246-410 was calculated by dividing a polarization intensity image by a total intensity image for a single spectral window. The color scale ranges from -30% to 80% polarization. The overlaid contours are of the multi-frequency total intensity image where contour levels begin at 10.1 mJy/beam and increase by factors of 2.

Chapter 2

Data Reduction Process

2.1 Observation Summary

For this project we were allocated three, six hour, observations of PKS1246-410 using the C, B and A configurations (3.4km, 11.1km and 36.4km, respectively) of the VLA. This large (u,v) coverage allows for high resolution images while remaining sensitive to the diffuse emission around PKS1246-410. All observations were observed from 8GHz to 10GHz, with the 2GHz bandwidth divided into 16 spectral windows containing 128MHz each, using 1 second integration time resulting in a theoretical sensitivity of $\sim 3\mu$Jy/beam. Due to the low declination of PKS1246-410 each observation was divided into two, three hour, observations. The B-configuration was the first to be observed in December 2013, followed by A-configuration in March 2014. We have recently scheduled the C-configuration observation which will be completed by January of 2015.

Each of the four observations used a single 8 minute run of 1331+305 (3C 286) as the flux and polarization angle calibrator, J1316-3338 as the phase calibrator with a scan time of 1.5 minutes on a cadence of 10 minutes to ensure phase stability through-

Table 2.1: Observational Parameters

Source	Date	Frequency (GHz)	Bandwidth (MHz)	Config.	Duration (hh:mm)
PKS1246-410	Dec. 15, 2013	9.0	2000	B	02:04
	Dec. 20, 2013	9.0	2000	B	02:04
	Mar. 11, 2014	9.0	2000	A	02:04
	Mar. 12, 2014	9.0	2000	A	02:04
	By Jan 2015	9.0	2000	C	04:08

out the observation, and finally OQ208 (J1407+2827) as the polarization calibrator observed 3 times (beginning, middle and end) for 4 minutes per scan to allow for polarization leakage calibration. A brief summary of the observations parameters can be seen in Table 2.1.

2.2 Data Reduction

The data reduction process was completed using three data reduction software packages: Common Astronomy Software Application (CASA), Astronomical Image Processing System (AIPS) and the difference mapping package - DIFMAP. The first step in the process was to calibrate the target source, PKS1246-410, through the nominal method of reduction using CASA. As discussed in Section 2.1 we used J1316-3338 as our phase calibrator. Our first step was to apply the pre-derived gain-curve correction of the antennas at 8-10 GHz, as well as to account for any antenna position corrections that may have occurred since the observation. We then set the fluxes of the flux calibrator using SETJY following the most recent standard of Perley-Butler 2013. We then performed an initial calibration to help remove the majority of the time dependent phase variations of 3C286. Next we accounted for the delay between

each antenna (on orders of nano-seconds) which would be interpreted as a baseline dependent phase difference. Having accounted for the phase solutions (at least initially) we then were able to derived the bandpass on our standard flux calibrator, 3C286, to remove receiver dependent effects. This bandpass calibration was then applied to all the calibrators before deriving the remaining phase and amplitude calibrations on each source which completed the parallel-hand calibration steps.

With the parallel-hand calibration complete we then had to derive the calibration for the cross-hand correlations. This was done by first establishing a frequency dependent flux model for our flux calibrator, 3C286. 3C286 is a well studied polarized source with an intrinsic angle of $\sim 67^{\circ}$ and a percent polarization of 12%. Using this a-prior knowledge we created a model by calculating the Stokes parameters for each spectral window. We then were able to find the delays present between the right and left polarizations signals. Using this we solved for the leakage terms of each spectral window, which is done by determining the amount of right-handed signal attributed to the left-handed signal and vise versa, by observing an unpolarized calibrator OQ208. After applying the previous calibration tables we determined the cross-hand polarization angle on 3C286 (67°) for each spectral window. We then used our known model of 3C286 to derive the fluxes of each calibrator based on their relative amplitudes to 3C286. To apply the derived calibration to our target we bootstrapped the derived solution of our phase calibrator (J1316-3338) on PKS1246-410. Throughout this step we flagged radio frequency interference (RFI) and edge channels which were problematic to the calibration process. Since our observations were higher frequency than many RFI sources present at the VLA, RFI was not a significant issue, however we were forced to flag an entire 128MHz spectral window at 9.275GHz due to RFI.

Due to the increased data-rates of the VLA, time and frequency averaging has become a necessity to the imaging analysis so that it can be completed in a reasonable timescale. The averaging process also has an added benefit of an increase in sig-

nal to noise per channel. To minimize chromatic aberration we used the equation $\left(\frac{\Delta\nu}{\nu 0}\right)\left(\frac{\theta_0}{\theta_{HPBW}}\right)$, where $\Delta\nu$ is the band width, ν is the frequency of concern, θ_0 is the angular extend of the source and θ_{HPBW} the Half Power Beam Width of the primary beam. Using this equation we referred to Table 9 in VLA Observation Status Summary (VLA OSS 2015A) to determine the amount of chromatic aberration (i.e. Bandwidth Smearing) we expect due to frequency averaging. We decided to allow for less than 5% reduction in peak response and as such we averaged the 64 channels within each spectral window (128MHz bandwidth) to 3 channels with varying bandwidth, as a result of differing edge channel effects.
The sampling time was also increased from 1 second to 5 seconds to have the minimal impact to the amplitude of 5% reduction in the peak response for a total reduction of 7 % due to both chromatic and time averaging. The time-average amplitude loss of an extended source can be determined by using the equation $(\theta\Delta t_{int})^2$, where θ is the distance from the phase center and Δt_{int} is the averaging time. A quick reference for determining the expected loss can be estimated in using Table 8 of the VLA Observation Status Summary (VLA OSS 2015B) assuming the source is well within the primary beam.

The four observations of the fully calibrated and averaged PKS1246-410 data were SPLIT into individual spectral windows from the multi-source file and the separate runs for each configuration were then combined together using the task CONCAT in CASA. Each spectral window of the B-configuration was then read into DIFMAP to be self-calibrated. DIFMAP has particular advantages in the task of self-calibration of a reasonable sized data set. DIFMAP allows the user to easily identify bad data, quickly plot baseline visibilities and interactively self-calibrate a dataset. As such we opted to use this package to create a model for each of our B-configuration spectral windows which was later used to calibrate the fully combined A+B data. Phase and amplitude self-calibration were completed for each spectral window then the visibil-

ities were outputted from DIFMAP. These fully calibrated visibilities were read into AIPS where a total intensity, Stokes I, image (RMS $\sim 20\mu$Jy/beam) was created for each B-configuration spectral window.

We then imported the A-configuration visibilities into AIPS and used the DBCON task to combine them with the B-configuration visibilities. The Stokes I image was then applied as a model for each spectral window using CALIB with a solution interval set to the sampling time of 5 seconds. The self-calibrated A+B visibilities were used to create I, Q and U images (20μJy/beam, 15μJy/beam and 15μJy/beam, respectively) with the same synthesized beam, set to that of the lowest frequency map ($1.06''$x $0.26''$at an angle of -4.41°).

Using COMB the Q and U images were combined to create a polarization angle and polarization angle error map for each channel (3 channels x 15 spectral windows = 45 polarization angle maps and 45 error maps). The 45 polarization angle maps and polarization angle error maps were assembled into a single cube using the task MCUBE. Due to the large number of polarization maps we had to develop a customized version of the RM fitting code used in previous studies (courtesy of Dr. Greg Taylor). The previous version would allow 10 input frequency planes but now we can use up to 60 different frequencies which will allow for the easy addition of more frequency planes in future studies. This cube was then read into the custom RM code where the rotation as a function of wavelength was fit for each pixel by a λ^2-law. The pixels in the RM image were flagged when the error in any of the polarization angle images exceeded 35 degrees. The resultant RM map can be seen in Figure 2.1 with an RM error map in Figure 2.2.

For comparison purposes a multi-frequency total intensity image was created using IMAGR in AIPS. Due to the low declination of PKS1246-410 and the fact that the observations were conducted in full A and B configurations the (u,v) coverage was far from uniform. As a result the restoring beam for the multi-frequency image was very elliptical with a 4:1 ratio of major to minor axis. This elongated restoring

beam must be considered when evaluating the morphology and general structure of PKS1246-410 throughout this study.

2.2.1 Cross-hand Calibration Issue

During the polarization calibration process it became apparent that the cross-hand correlations for the B-configuration observation on Dec. 20 were varying as a function of frequency differently than that of the parallel hands. This problem became apparent when attempting to calibrate the leakage term. Each spectral window demonstrated a different frequency dependent trend and were discontinuous with one another. Figure 2.3 shows the expected correct calibration seen for the second B-configuration run while Figure 2.4 shows the effect of the discontinuous frequency dependent variation. Unable to remedy this anomaly we opted to not use the cross-hand correlations, Q and U, for this observation. The parallel-hands remained unaffected and were used in the total intensity maps.

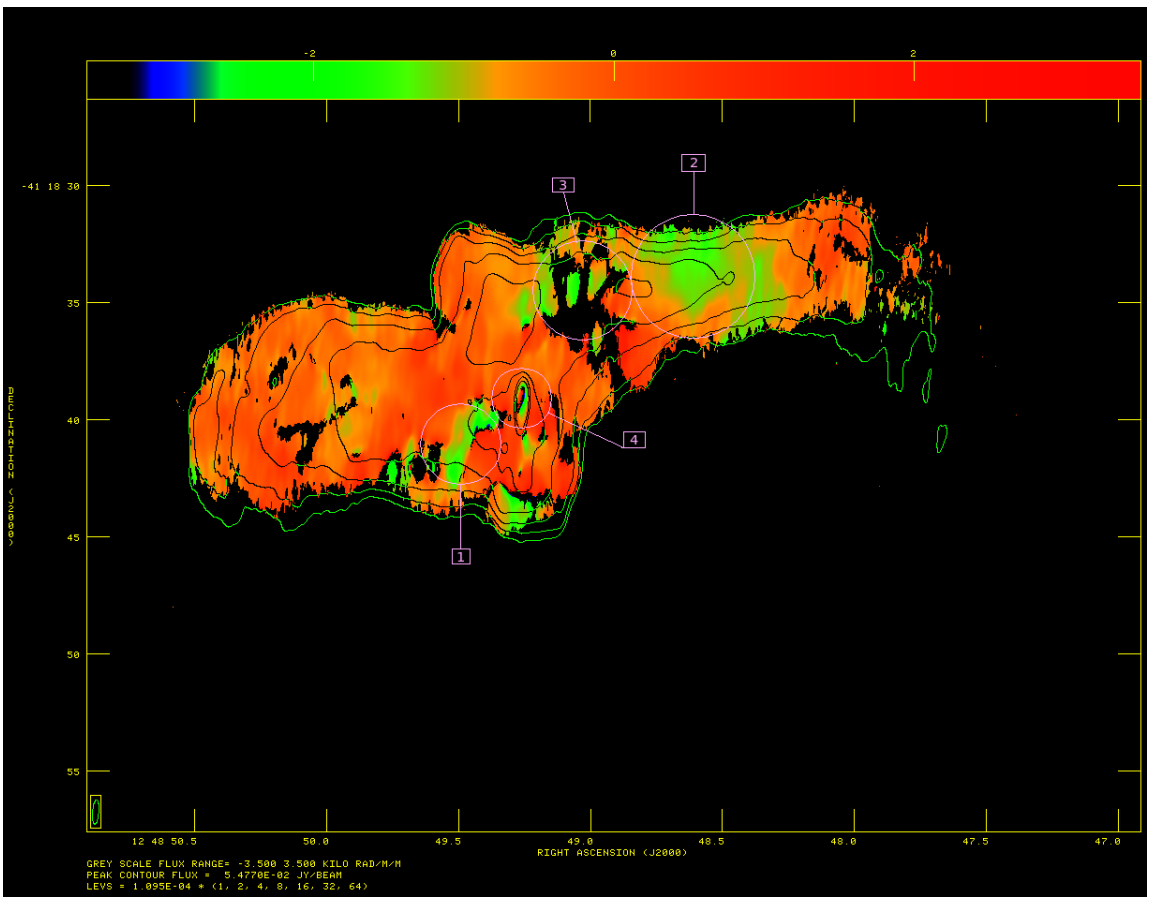

Figure 2.1: In this rotation measure map the color scale is in units of kilo rad/m^2. The contours are of the multi-frequency total intensity image where contour levels begin at 10.1 mJy/beam and increase by factors of 2. Regions of enhanced RMs which are discussed in Section 3.2.3 are numbered for convenience. The bottom left corner also graphically indicates the restoring beam size and angle.

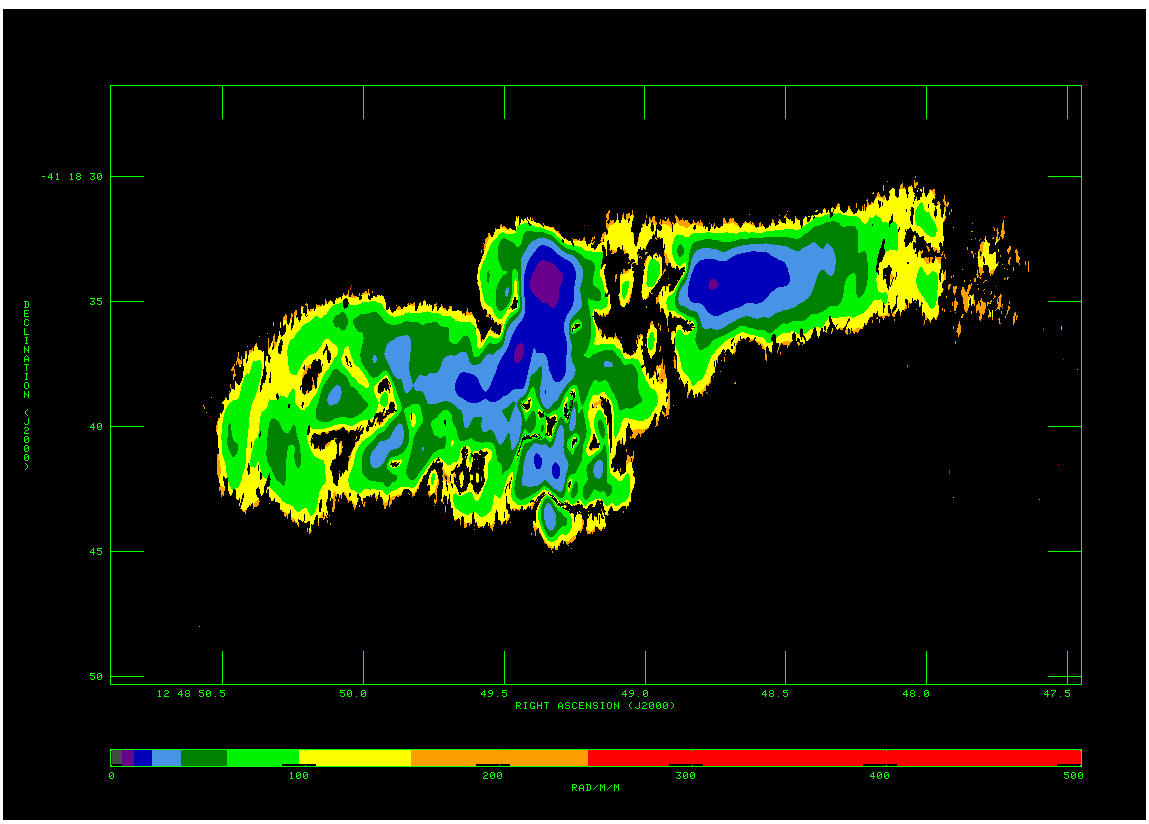

Figure 2.2: The RM noise image shows the obtained errors of the rotation measures from Figure 2.1. The color scale shows values from 0 rad/m^2 to 500 rad/m^2.

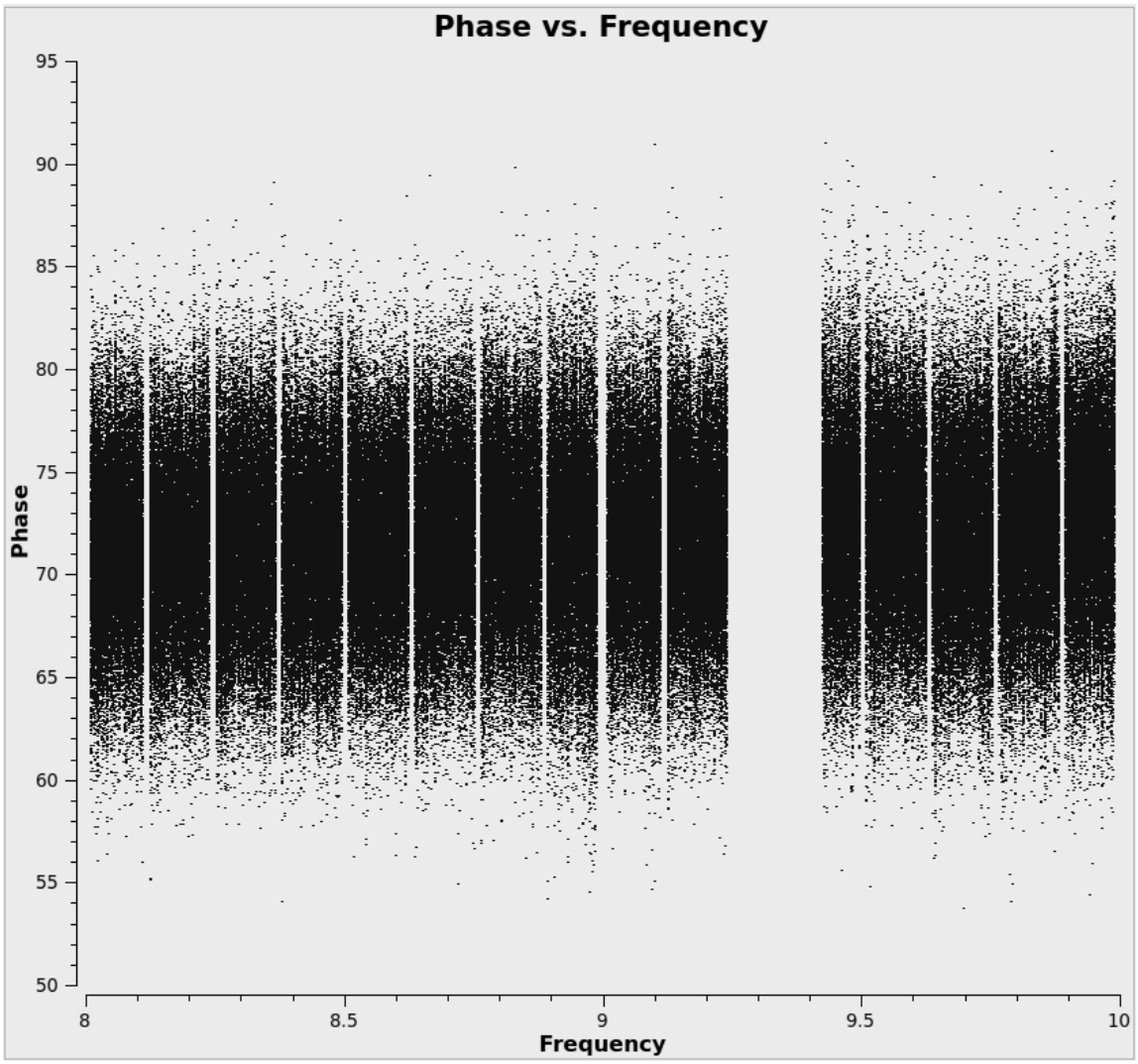

Figure 2.3: Calibrated cross-hand data plotted as phase vs. frequency on 3C286 for Dec.15,2013 observation. This plot demonstrates the expected result from a properly calibrated dataset.

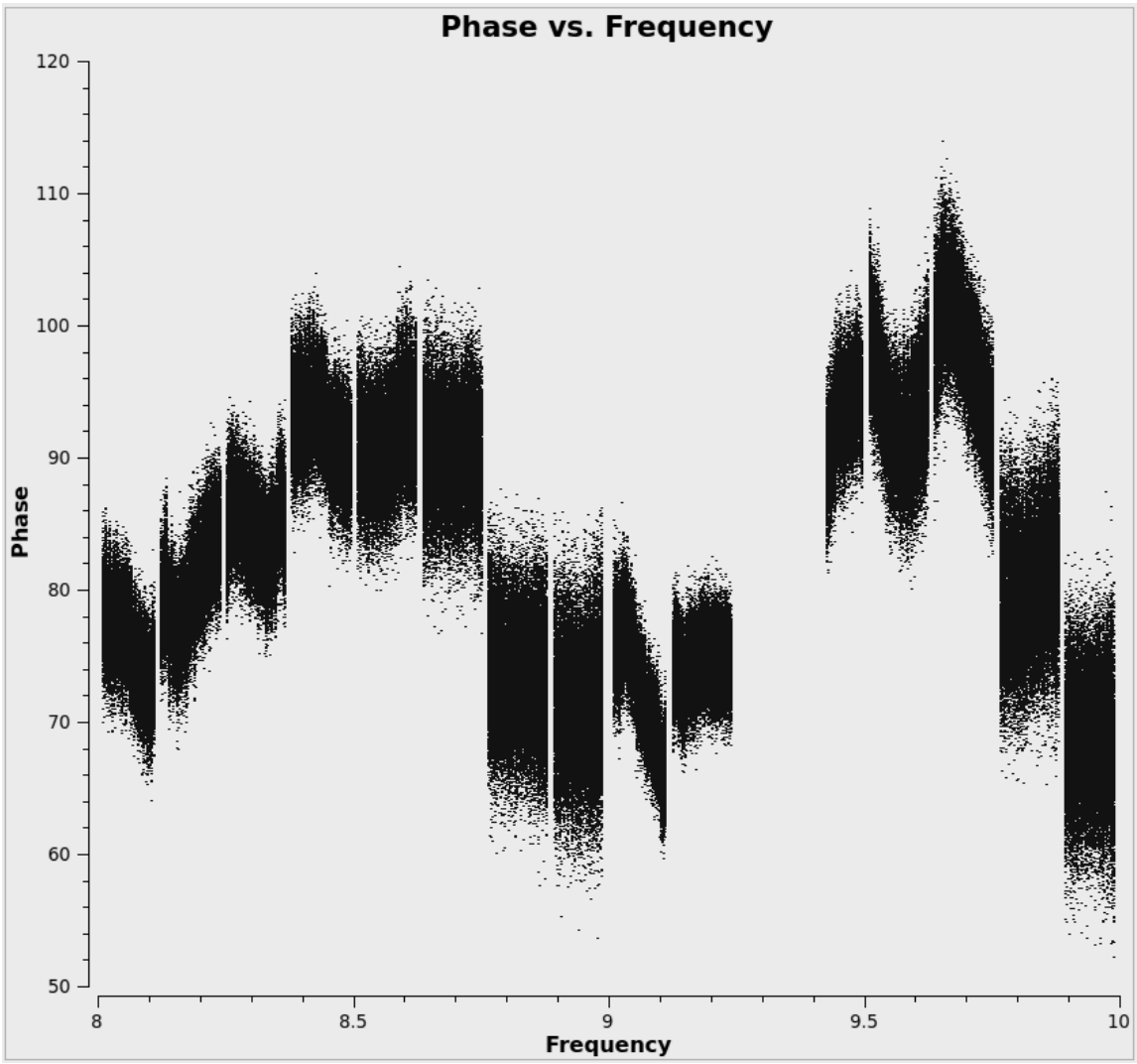

Figure 2.4: Calibrated cross-hand data plotted as phase vs. frequency on 3C286 for Dec.20,2013 observation. In this plot we can quickly see that the typical calibration method is insufficient due to a variation of the cross-hand calibration as a function of spectral window.

Chapter 3

Results & Analysis

In this section we present the highest angular and spatial resolution rotation measure study of the PKS1246-410 to date. The recently increased bandwidth capabilities of the VLA allow us to probe a larger phase space of rotation measures than ever before on PKS1246-410. Here we present the results from our study of the combined A and B-configuration for a total of 8.25 hours on source across approximately 2GHz of bandwidth.

3.1 Total Intensity Maps

First we will discuss the total intensity images. Previous work has documented in detail the structure of central radio source PKS1246-410 (Taylor 2002, Sanders 2002, Taylor 2007). The distinct morphology can be seen in Figure 3.1 where the radio arms are bent back. Previous work has attributed this bent lobe structure to interaction with the diffuse ICM. These studies noted the radio lobes of PKS1246-410 are coincident with X-ray "holes" known as radio bubbles or ghost bubbles. These cavities are interpreted as low density areas that were inflated during a time

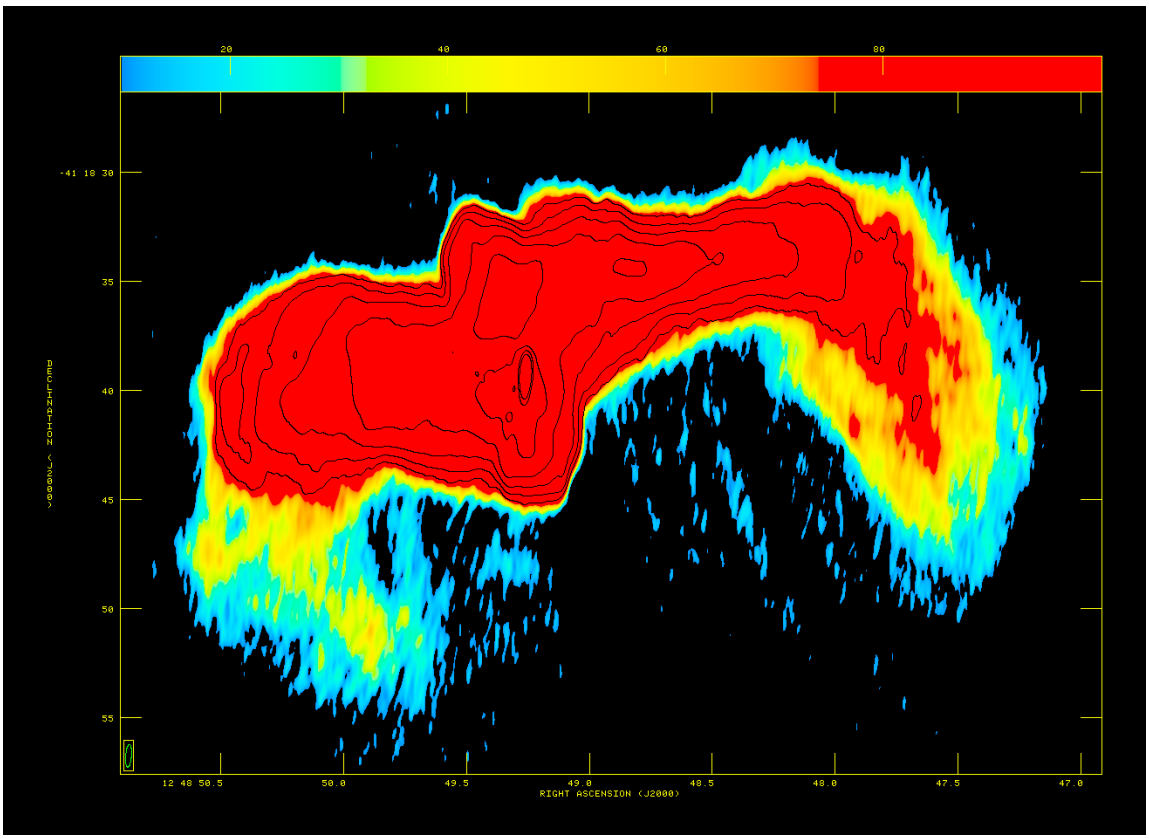

Figure 3.1: The color scale shows the diffuse total intensity radio emission ranging from 20-100μJy/beam. The contours are of the multi-frequency total intensity image where contour levels begin at 10.1 mJy/beam and increase by factors of 2. The bottom left corner also indicates restoring beam size and angle.

of activity and since have detached from the central region on either side due to the buoyancy of the contained gas (Hatch et al. 2006). As discussed in Section 2.2 we use a synthesized beam of 1.06″x 0.26″at an angle of -4.41° as compared to previous studies at lower frequencies which had a synthesized beam of 2.1″x 1.2 ″at an angle of 19°. Due to the improvements of the VLA the increased bandwidth has allowed for better sensitivity of images, such that our total intensity image (Figure 3.1) has a root-mean-squared (RMS) value of 3μJy/beam compared with 0.3mJy/beam in previous studies.

3.1.1 Spectral Index Map

We have obtained a spectral index map of PKS1246-410 using Stokes I images of the first and last spectral windows, 8.02 GHz and 9.91 GHz, respectively. Both spectral window were cleaned to a RMS of 20μJy/beam with the same restoring beam of 1.06″x 0.26″at an angle of -4.41°. These two images were combined using task COMB in AIPS with a clipping of $2\sigma = 40\mu$Jy/beam for both images. The resultant map can be seen in Figure 3.2. Disregarding the outlining structure of the source where the spectral index noise is greater than 1, thus unreliable, we found an average spectral index of $\alpha \sim -1 \pm 0.25$. The spectral index appears to remain very stable throughout the source with two notable exceptions. The first exception is the spectral indices on the extremities are $\alpha \sim -2$, however, due to low signal to noise in these regions the errors are ≥ 1. Therefore, it is difficult to determine whether the obtained spectral index is due to interaction with the ICM or if the extremities follow the same trend as the interior region. The second point of interest is the region about the core. The obtained spectral index from the core region has a mean value of -0.56 ± 0.13. This result is consistent, albeit less precise, with the spectral index found by Taylor et al. (2006) where they fit the radio flux spectral of the nucleus from 1.4 GHz to 43.3GHz with the Very Long Baseline Array (VLBA) and found spectral index of $\alpha = -0.55 \pm 0.04$.

3.2 Rotation Measure

To further understand the morphology of the ICM in the context of galaxy clusters we have investigated the sub-structure in the obtained RM map. In this section we will discuss qualitatively the structure of the observed rotation measure and further discuss in the next section how these results impact our understanding of the ICM. We further focus on four distinct regions that demonstrate enhanced rotation measures

and quantitatively discern what they tell us about on the intracluster environment. Throughout this section we will be referring to RM and RM error maps found in Figures 2.1 and Figure 2.2, respectively. For ease of reference we have defined the four regions of enhancement to be discussed later in the section in Figure 2.1.

3.2.1 Magnetic Field Models

Using the equations from Section 1.5.1 we can offer magnetic field estimates required to create the RMs measured, assuming two different types of models. The first model assumes a very simplistic case where all the variables in Equation 1.2 are uniform. Therefore using the electron density model from Taylor et al. (2006) where $n_e = 0.099 cm^{-3}$ and $dl = 10$kpc then Equation 1.2 becomes:

$$B_{||} = \frac{RM}{803.88} \quad [\mu G] \tag{3.1}$$

where RM is the observed rotation measure for the specific region in rad/m^2. We can also use a more complex model in which we assume the magnetic field is tangled with a cell size of 1 kpc as in Equation 1.4. We can further reduce Equation 1.4 by using β model parameters found from X-ray studies of Centaurus (Taylor et al. 2002): $\beta = 0.39 \pm 0.01$, $n_e = 0.099 \pm 0.001$cm^{-3} and $r_c = 5.4 \pm 0.3$kpc. Using these parameters along with some reasonable cell size of Λ_C=1 kpc which is estimated by the observed variations sizes in RMs. We also can assume the radio source lies at the core with very little projection effect, resulting in K=441 and $r << r_c$ (Taylor et al. 2002), due to a correlation between the radio lobes and X-ray bubbles discussed in Section 3.1. Using these values we can reduce Equation 1.4 to a very simple formula, dependent only on the distribution of RMs in a region of interest:

$$B = 8.2(10^{-3})\ \sigma_{RM} \quad [\mu G] \tag{3.2}$$

3.2.2 Average structure of PKS1246-410 RM map

First we will focus on the average structure and reoccurring trends seen in the obtained RM map. This RM map exhibits values ranging from -3500rad/m^2 to 3500rad/m^2 for good fits and low noise levels (3σ = 125.2 rad/m^2). In Figure 3.3 we present the distribution of RMs for the entire radio source. As can be seen in this histogram plot the mean of the distribution occurs at -391 rad/m^2. However, one would expect to see a Gaussian distribution of RM dispersions centered around zero as discussed in Section 1.5.1 (Felten 1996). This trend has been also seen in previous studies of PKS1246-410 conducted by Taylor et al. (2002) in which they reported a multiple peaked distribution with a mean of -360 rad/m^2. The more Gaussian like structure in our results, as compared to Taylor et al. (2002), is most-likely due to a higher signal to noise and increased angular resolution of our RM map. Taylor et al. (2002) suggested the negative mean seen in both studies could indicate that the distribution is dominated by the contributions of a small number of cells.

We would like to point out that the sub-structure in the RM map is stable on arcsec (100s pc) scales across the source as opposed to previous results in Taylor et al. (2002). This smoother variation, similar to the RM distribution discussed prior, is likely due to the increase angular resolution and sensitivity. If the RMs vary too quickly across the synthesized beam they will create a less confident λ^2-law fit due to ambiguity of RMs within the beam. Also, the increased sensitivity allows for a more confident fit of the RMs throughout the source due to smaller polarization angle errors. Since we are probing the source on scales less than the RM variations, a well behaved RM would expect to be described by a Gaussian distribution as seen in Figure 3.3.

Using the distribution of RMs in Figure 2.1 we can estimate the magnetic field required to create the observed rotation from the two models described in Section 3.2.1. In the case of the uniform magnetic field model we will use the largest RM enhance-

ment found of $RM = -2500\text{rad/m}^2$ to find the parallel component of the magnetic field strength to be $B_{||} = 1.87\mu G$. Then assuming the total magnetic field is related by $B = \sqrt{3}B_{||}$ (Taylor et al. 2002) we find a magnetic field of $3.23\mu G$. For the second model we use the FWHM of the distribution of RMs derived in Section 3.2.3 to determine the dispersion RMs $\sigma_{RM} = 667.8\text{rad/m}^2$ to estimate the magnetic field. In the tangled magnetic field model we find a magnetic field strength of $B = 5.4\mu G$ across the entire source.

3.2.3 Enhancement regions and possible depolarized zones

In this section we will discuss regions of enhanced RMs and possible depolarization regions. Approximating the histogram of the distributions for the obtained RMs as a Gaussian (Figure 3.3) we have determined a Full-Width-Half-Max (FWHM) of 668 rad/m^2 which corresponds to RMs from -1059 rad/m^2 to 279 rad/m^2. This distribution is assumed to be representative of a Gaussian distribution about a mean of -391 rad/m^2 as is predicted by Equation 1.3 describing RM dispersion. Given a Gaussian type distribution we found a standard deviation of 291 rad/m^2. Therefore we quantify a region of enhanced RM to be extended regions that deviate at least 3σ from the mean value over arcsec scales, corresponding to $\lesssim$ -1287 rad/m^2 or $\gtrsim$ 505 rad/m^2. By this definition we found four extended regions of possible enhancement. For each region we show a representative sample of the RM fits throughout the region of enhanced RMs.

Region 1: Tube of Enhancement South-East of Radio Core

South-East of the core we find a tube like structure of enhanced RMs. The mean value is -1250 rad/m^2 which extends along the major axis for 4 arcsec (800 pc) and the

minor axis for 1 arcsec (400 pc). To quantify this enhancement we show in Figure 3.4 a RM slice perpendicular to the major axis of the tube. In Figure 3.5 we show a grid of the RM fits from the central most enhanced pixels of the tube to ensure that the fits are accurate and continue to obey a λ^2-law. Using the distribution within this region we can estimate the magnetic fields required to create such a rotation measure. Within this region we find a max RM of -1750 rad/m^2 which using Equation 3.1 we find a magnetic field strength of 3.77μG assuming a uniform model. Assuming a tangled magnetic field model we find a magnetic field strength of 0.22μG when using Equation 3.2.

Region 2: Gradient across the western jet

Another region of enhanced RMs occur on the western arm of the radio source. As seen in Figure 2.1 the northern part of the western arm exhibit RMs up to -1500rad/m^2 while the southern part of the arm approaches 0 rad/m^2. To show this effect clearly we have taken a north-south RM slice across the western arm which can be seen in Figure 3.6. It is worth noting when extrapolating from this graph one must realize that the noise increases on the extremities of the source which will result in less confident RM fits. This effect can be seen in Figure 2.2 where the noise on the interior region errors are a fraction of the extremities. Therefore we will focus on the inner 4.5$''$ which shows a steep negative trend from around -1500 rad/m^2 in the north to around -250 rad/m^2 at the southern part of the arm. Using the maximum RM of -1500 rad/m^2 in this region we find a magnetic field strength of 4.30μG. Using the distribution of RMs in this region we calculate a tangled magnetic field strength of 1.47μG.

Region 3: Enhanced RM Knot at the Beginning of the Western Arm

The third region exhibiting enhanced RM values is located at the beginning of the western arm. Previous studies have suggested this region to be a possible location for depolarization, most-likely due to dense soft X-ray emitting gas in front of the region (Taylor et al. 2007). Depolarization occurs when the Faraday screen rotating the wavefronts becomes too thick and randomize (i.e. depolarize) the polarized emission. Our high angular resolution could help to give validity to that argument by noting that we observe knots of enhanced RMs surrounded by absent RM regions. Figure 3.7 shows that we have found RMs up to -2100 rad/m^2 that obey the λ^2-law. These knots are not conclusive proof of a depolarized region, however the high RMs might indicate dense regions which could be denser around the knot where the RM fits are unavailable possibly due to depolarization. Once again we will use the highest RM, -2100 rad/m^2, to estimate a magnetic field strength of $4.52\mu G$ using the uniform magnetic field model. Assuming a tangled magnetic field we find a magnetic field strength of 0.76 μG based on the distribution of RMs in this region of enhancement.

Region 4: Radio Core

The final region which we would like to discuss is the radio core. While our study was in no means tailored to observe the small radio core, our A-configuration observations have provided us the opportunity to probe the core on sub-arcsec scales. There are two distinct features we would like to note located around the core region. The first feature is an open-annulus structure of absent rotation measures around the radio core. This could be an artifact of the imaging process where we were unable to completely fit the visibilities at the core due to the very high flux compared with the rest of the radio source, however, since the polarized intensity of the core is

comparable to the rest of the source it is unlikely that this is the case. Another more intriguing explanation could be that this annulus is a region of depolarization due to high densities located less than 100pc around the radio core. To attempt to determine the validity of this explanation we present Figure 3.8 showing the RM fits within the core and Figure 3.9 on the outer edge of the core. As can be seen from these two images there is a transition over very few pixels where the RMs transition from a positive to negative slope. While the fits are well behaved and mostly follow a λ^2-law, the noise becomes a factor at the boundaries making it difficult to determine how significant the enhancement of RMs are at the core. We can also compare the unfit RM regions around the core to that of the the polarization percentage map in Figure 1.1. We can see around the core there is an annulus of no polarization which would support our argument of depolarization.

We can again estimate a uniform magnetic field strength of 4.30 μG is required to create the maximum rotation measure of -1500 rad/m^2 observed in this region. However, if we use the tangled magnetic field model we find a magnetic field strength of 2.82 μG for this region of enhancement.

3.2.4 Source Magnetic Field

Our RM fitting code discussed in Section 2.2 also determines the local orientation of the magnetic field (corrected for Faraday Rotation) based on the RM fits. Using the obtained RMs our customized code removes the calculated Faraday Rotation from the observed polarization angle, pixel by pixel, to determine the source magnetic field. As can be seen in Figure 3.10 the magnetic fields are well ordered along the western arm until reaching the low polarization strip at the beginning of the arm. Here the magnetic fields appear to be pointing radially outward from Region 3 in Figure 2.1. The magnetic field vectors appear to be well ordered and follow the total intensity contours closely in a relatively uniform manner aside from the

aforementioned Region 3. The regularity of the derived magnetic field is expected for extended sources which further indicates that we have properly account for the Faraday Rotation observed for PKS1246-410.

3.3 Analysis & Summary

Our study has allowed for the opportunity to observe PKS1246-410 at high angular resolutions (arcsec scales) and sensitivities ($\sim \mu$ Jy/beam). We have shown that the extended structure of the PKS1246-410 possess expected spectral index values which indicate synchrotron radiation. There are also possible indications of steeper spectrum emission along the extremities of the radio source: $\alpha \sim -2$. However, since our bandwidth is limited to 2GHz it is not tailored to a spectral index analysis resulting in significant noise on these extremities, $\alpha \sim \pm 1$. We have observed that the core spectral index result is slightly flatter, $\alpha = 0.56 \pm 0.13$ than what is observed for the average source spectral index, $\alpha = 0.56 \pm 0.13$. This result, albeit less precise, agrees with previously publish results from Taylor et al. (2006).

Using the total distribution of RMs we find that our results of the magnetic field strengths ($B = 3.23\mu G$ and $B = 5.4\mu G$ using uniform and tangled models, respectively) tend to agree with previous estimations of the magnetic field for the Centaurus Cluster of $B = 8\mu G$. These predictions are on the border for estimates of non-cool-core clusters ($1 - 10\mu G$) and strong cool-core cluster ($10 - 40\mu G$) magnetic fields strengths. Since the estimate is less than that of a typical cool-core cluster we would expect the magnetic fields to have a larger coherent structure than the randomly oriented cells in the tangled magnetic field model suggests. This greater understanding of the behavior of the RM distribution seen from PKS1246-410 could help us to understand on what scales the magnetic fields in cluster vary. To do this we have probed the sub-structure of the magnetic fields by focusing on four enhancement

regions.

The magnetic field strength derived for each enhancement regions have found that the uniform magnetic field model is in good agreement with the total RM distribution estimates of the magnetic field strength. The distribution of RMs in the enhancement regions are less disperse than the total distribution causing a lower value estimate for the magnetic field strength, when using the tangled magnetic field model. This lower value indicates that the magnetic field are less randomly oriented on these 100s parsec scales as compared to the entire radio source of 10s kpc. We would expect the tangled magnetic field model to be more applicable when sampling multiple randomly oriented cells, as is the case for the total RM distribution. This result can help use to understand the magnetic field coherency size which from our results on the order of arcsec (100s pc) or larger, due to the little dispersion of RM values within these regions.

We also can use our results to further argue for the existence of depolarized regions present around Region 3 and Region 4. If we refer to Figure 1.1 we can see that the regions we identified as possible depolarized zones due to proximity of high RMs, are regions of unpolarized signal. However, this could also indicate that the source itself is not polarized in these regions. To further understand the proper explanation for these regions of low polarization we will need to investigate other wavelengths, such as X-ray, at a higher sensitivity and resolution to determine if these regions of enhancement correlate with any density enhancements.

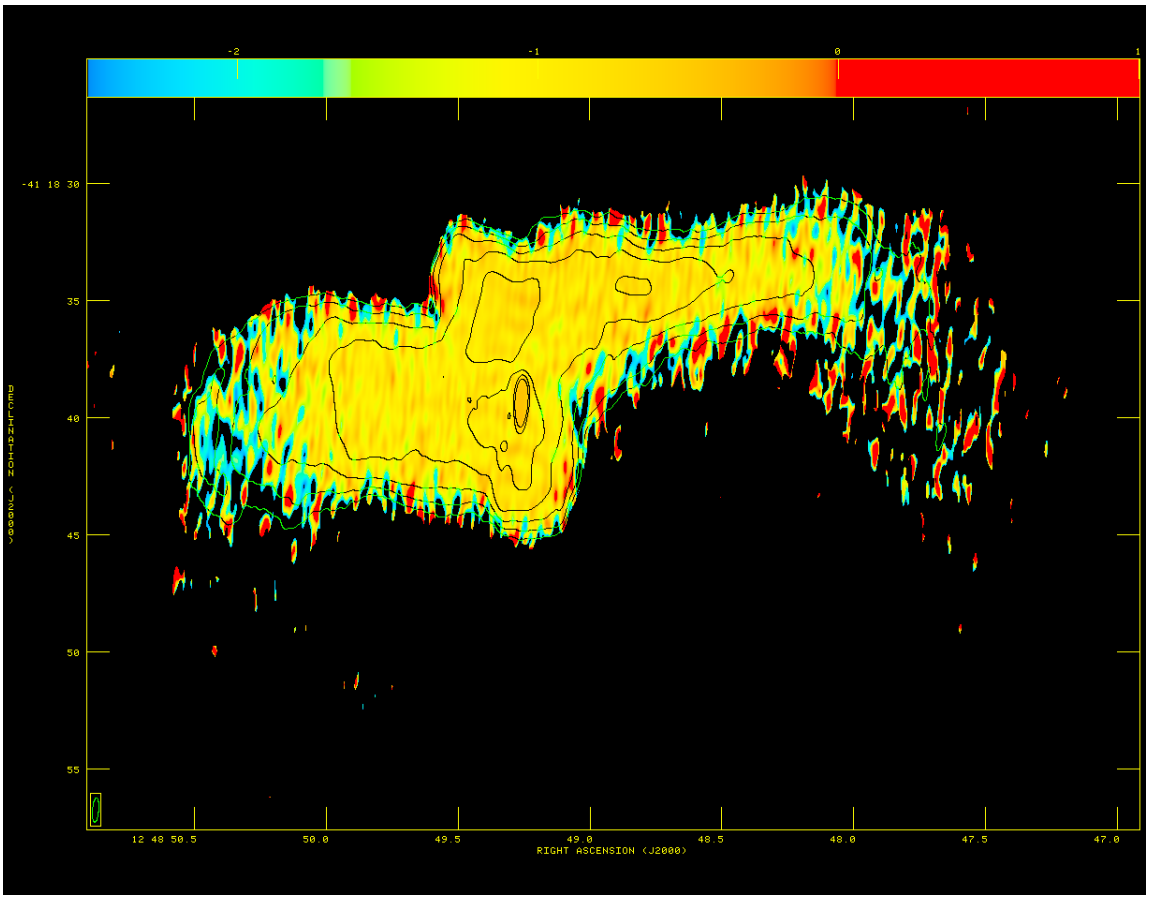

Figure 3.2: Color indicates spectral index values from α=-2 to 1. The contours are of the multi-frequency total intensity image where contour levels begin at 10.1 mJy/beam and increase by factors of 2. Regions of enhanced RMs which are discussed in Section 3.2.3 are number for convenience. The bottom left corner also indicates restoring beam size and angle.

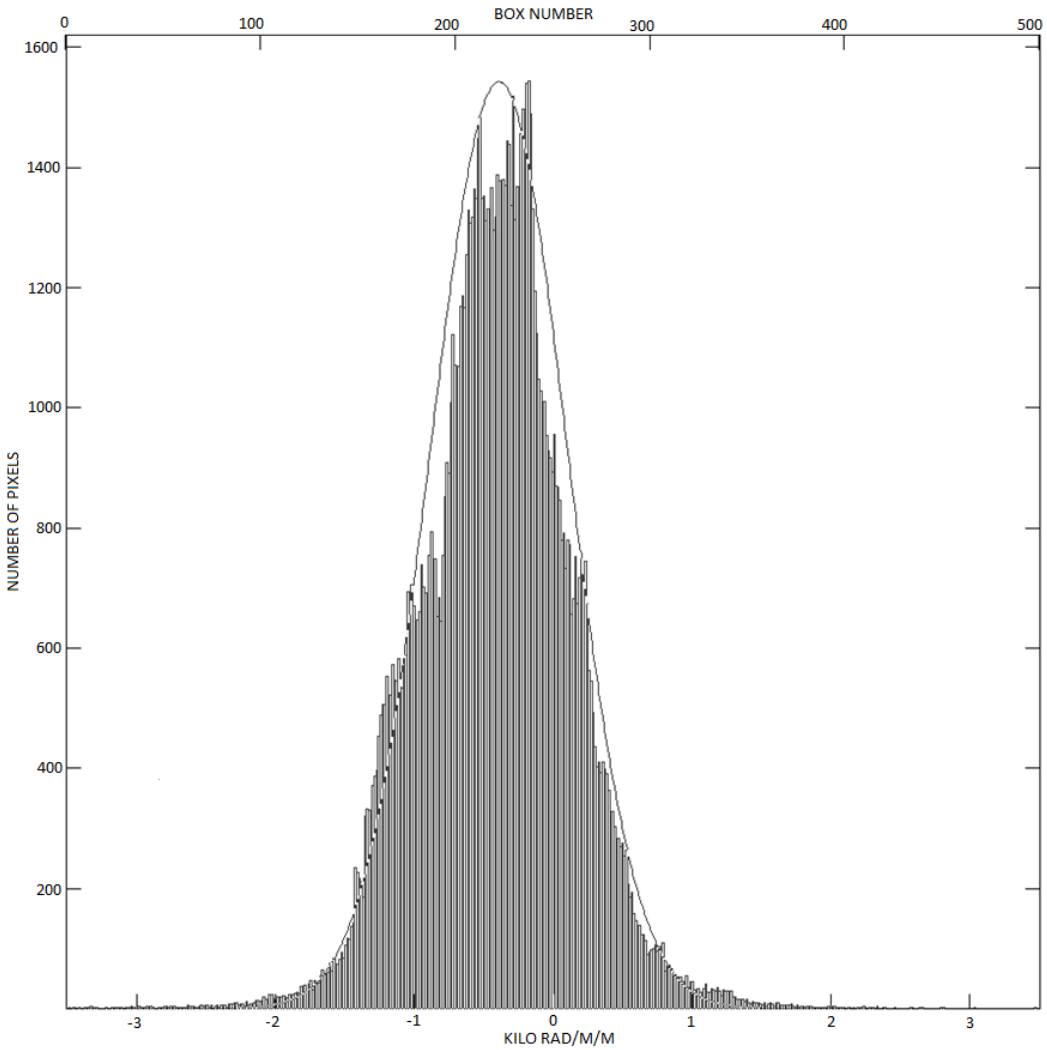

Figure 3.3: Histogram of rotation measure values across the entire radio galaxy.

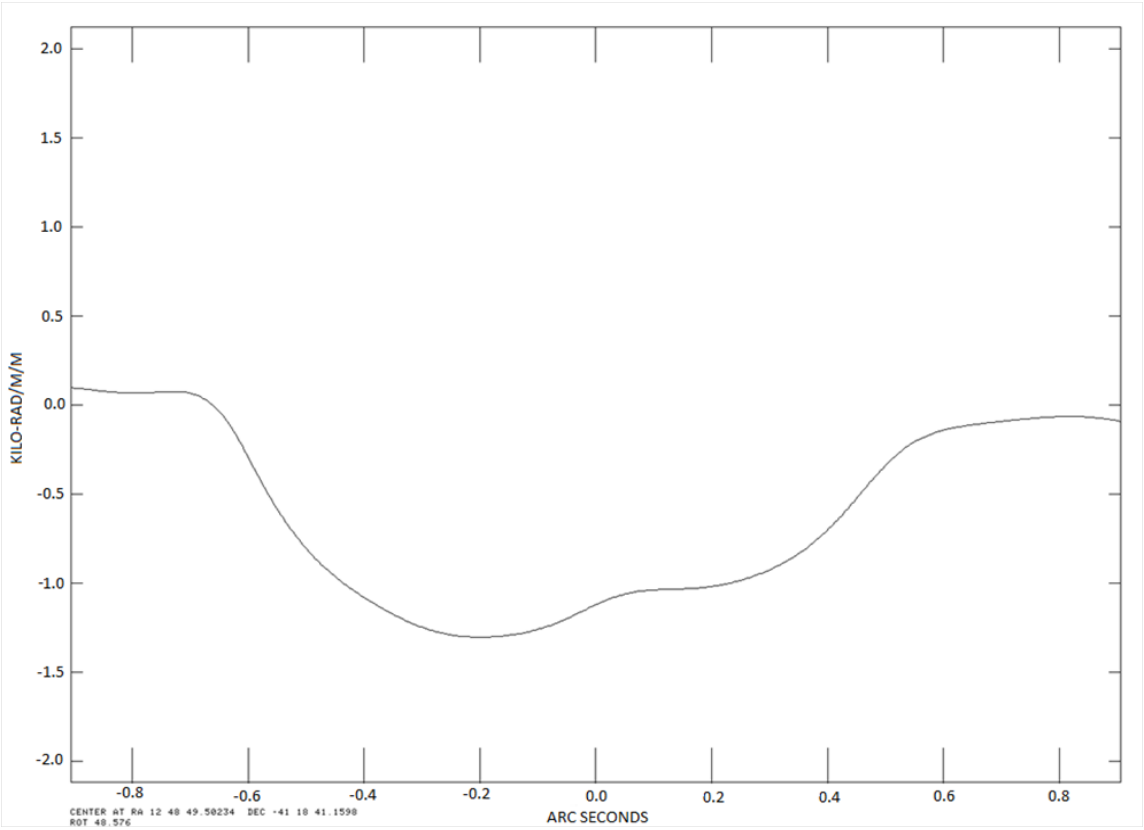

Figure 3.4: Rotation Measure slice along the minor axis of region 1 to show the enhancement of RMs.

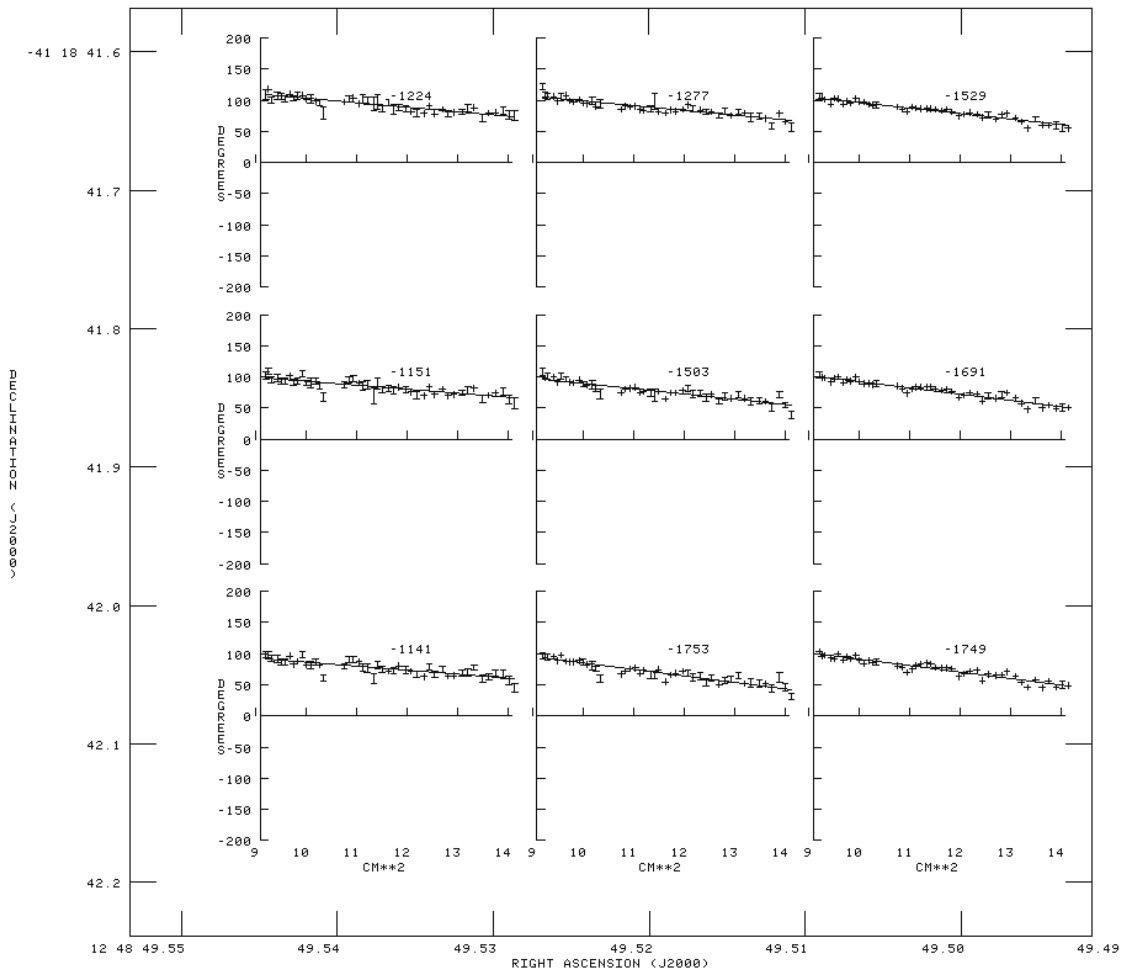

Figure 3.5: The plot above shows the extracted RM fits created by RMCUB from region 1. Each panel is the RM fit extracted across a 5 by 5 pixel increment. This plot demonstrates how well behaved the fits are within this "tube" of enhancement.

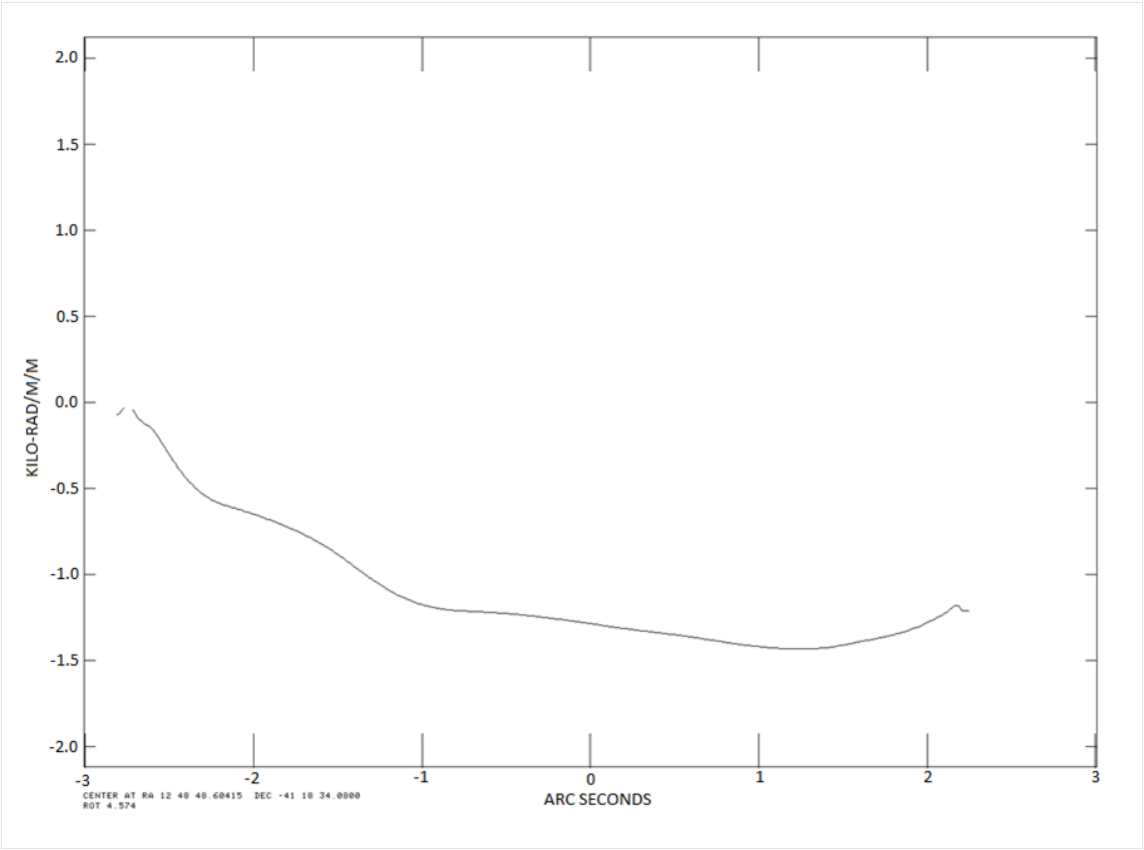

Figure 3.6: Above is a north-south Rotation Measure slice of region 2 which demonstrates the gradient of enhancement in the western arm.

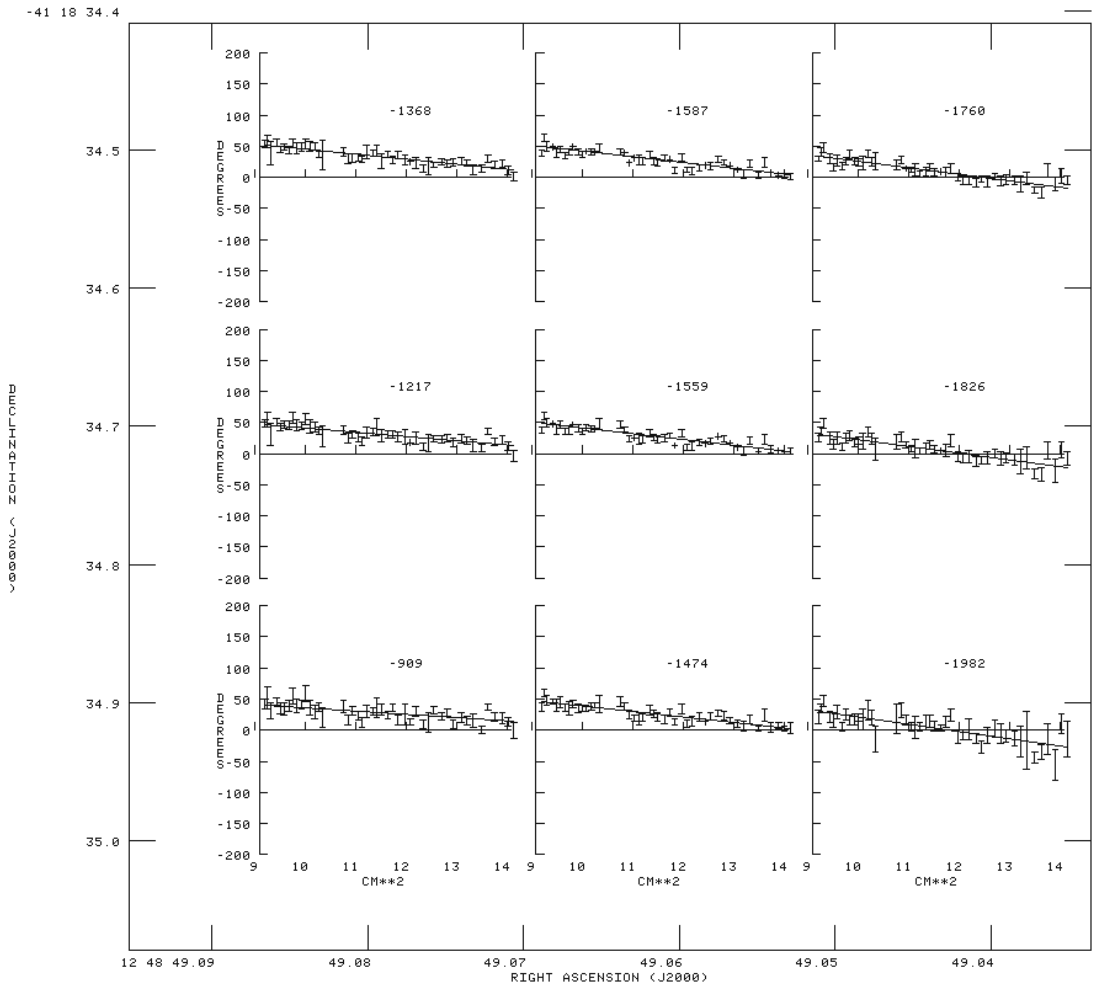

Figure 3.7: The plot above shows the extracted RM fits created by RMCUB from region 1. Each panel is the RM fit extracted across a 5 by 5 pixel increment. In this figure you can see a slight gradient from the bottom left to the top right.

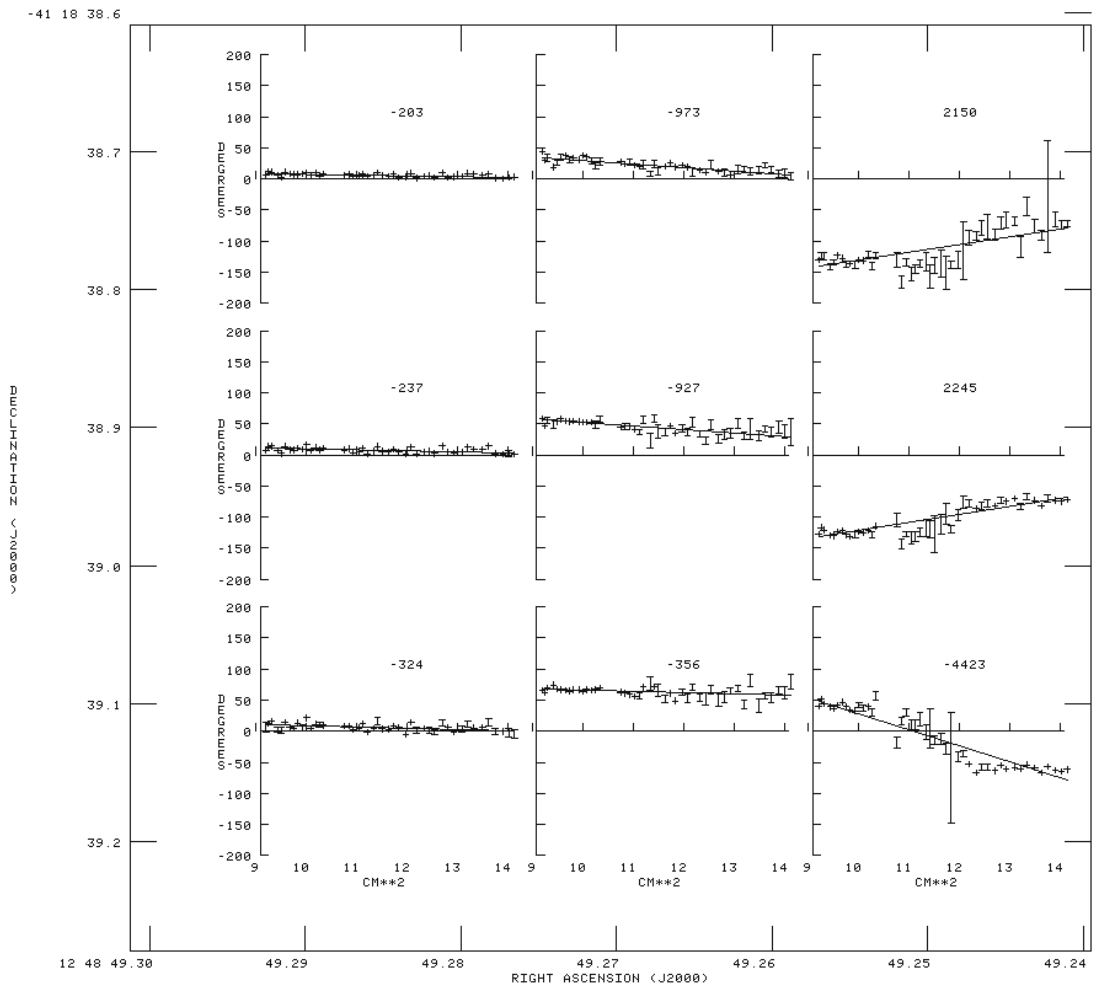

Figure 3.8: The plot above shows the extracted RM fits created by RMCUB from the inner core in region 3. Each panel is the RM fit extracted across a 2 by 2 pixel increment.

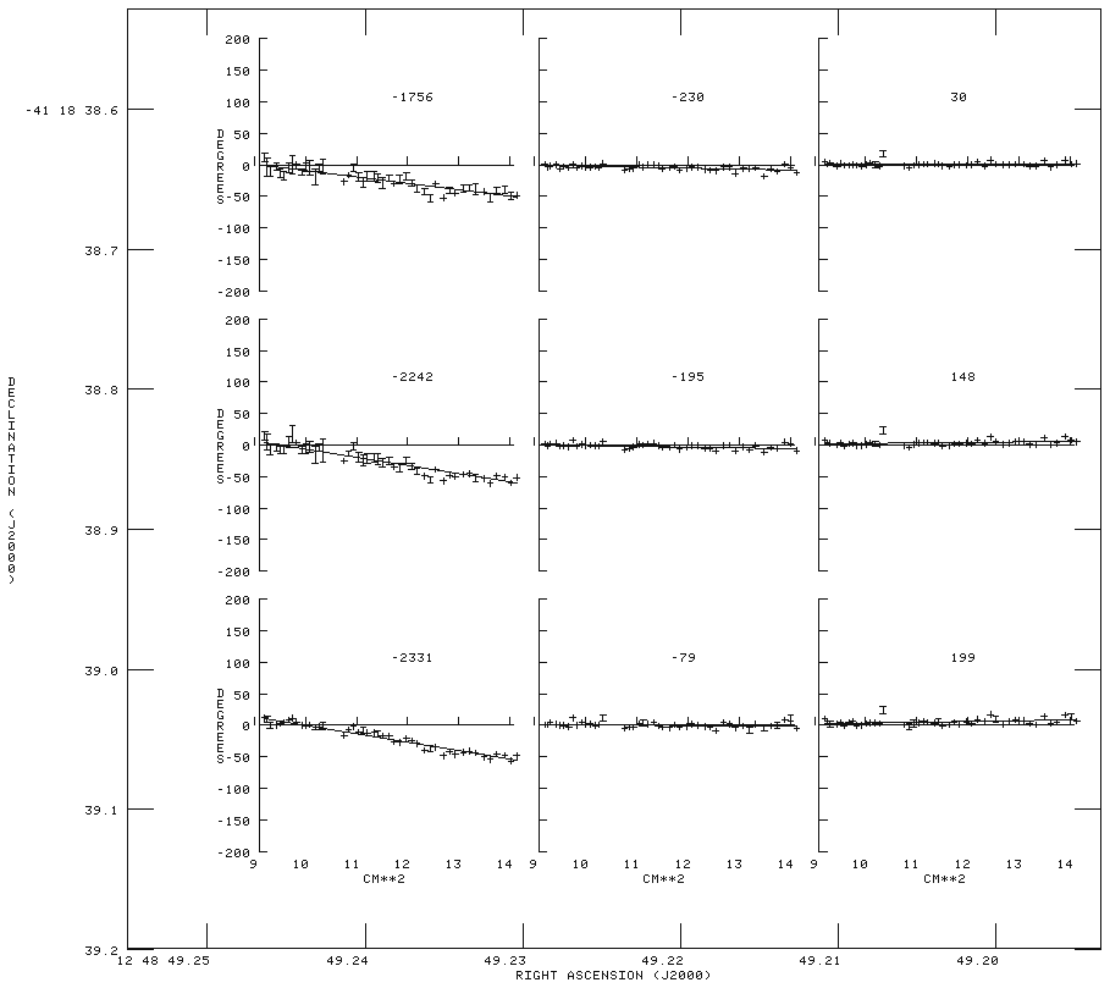

Figure 3.9: The plot above shows the extracted RM fits created by RMCUB from the outer edge of the core in region 3. Each panel is the RM fit extracted across a 2 by 2 pixel increment.

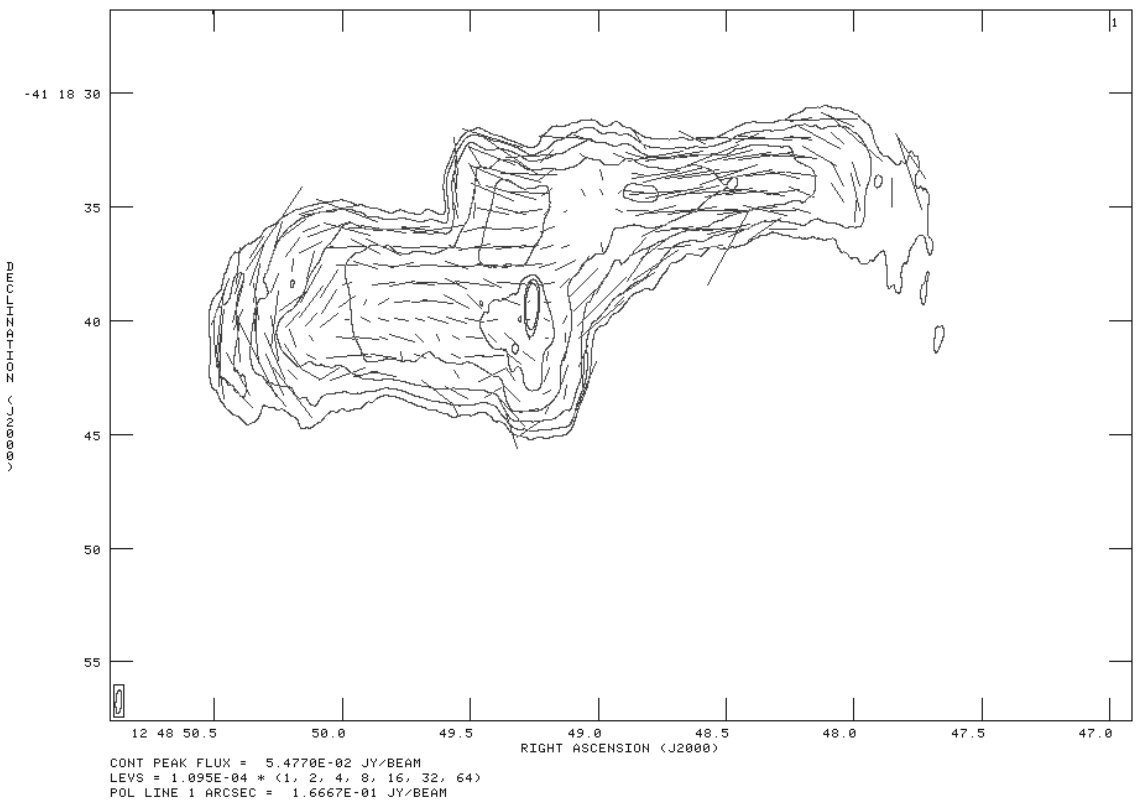

Figure 3.10: The above figure shows the magnetic field lines derived from the Rotation measure fit where a 1 arcsec line is equivlent to 0.167 Jy/Beam. Overlaid is a multi-frequency total intensity contour where contour levels begin at 10.1 mJy/beam and increase by factors of 2. The bottom left corner also indicates restoring beam size and angle.

Chapter 4

Conclusion and Future Work

4.1 Conclusion

To date this is the deepest radio study conducted of the central galaxy in the Centaurus cluster. The new advancements of the VLA which increased the bandwidth has greatly aided in the efforts to understand the ICM in the center of the Centaurus Cluster and hopefully other cooling core clusters. Clusters could in theory create large scale magnetic fields which interact with the ICM to produce magnetic fields of $\sim \mu G$ strengths, which seems supported in our study. Understanding the level of turbulence within these environments can impact our models for the merging and thus evolution of galaxy clusters. If we understand how galaxy cluster evolve over time we will gain further insight to the initial conditions present moments after the big band that resulted in the Cosmic Web structure we see today.

4.2 Future Work

Future work will entail combining the VLA C-Configuration to increase the time on source from 8 hours to 12 hours. This increase in time on PKS1246-410 will result in a multi-frequency synthesis image with theoretical 1σ sensitivity of 3μJy/beam. However, even more importantly is the C-Configuration will allow for the probing of even more diffuse structure in the arms of the radio galaxy.

Combining these results with all other previous VLA studies of PKS1246-410 would help to further investigate both diffuse and high angular resolution structure. Previous studies have combined frequencies ranging from 323 MHz to 43.3 GHz (Taylor et al. 2006). This large bandwidth combined with our 8 hours of exposure time on source could help further constrain the RM fits of PKS1246-410 to great sensitivity. Using this increase in sensitivity combined with large frequency coverage we could also investigate the presences of steep-spectrum radio sources, such as mini-halos, at the center of the Centaurus Cluster.

One final goal for this research will be to combine our radio results with the recently obtained Chandra data currently being reduced and analyzed by collaborator Dr. Jeremy Sanders. This multi-wavelength approach will help to understand more properties within the ICM at the center of the Centaurus Cluster, such as, velocity distribution and its viscosity. Understanding such properties will help to determine what underlining physics are at play in these very extreme environments at the center of a cool-core.

References

[1] Burn B. J. 1966, MNRAS, 133, 67

[2] Carrilli C.L., Taylor G. B., 2002, Annual Reviews of Astronomy and Astrophysics, 40

[3] Edge A. C. 2001, MNRAS, 328, 762

[4] Felten J. B., 1996, in Trimble V., Reisenegger A., eds, ASP Conf. Ser. 88, 271

[5] Ferrari C., Govoni F., Schindler S., Bykov A. M., Rephaeli Y. 2008, Space Science Reviews, 134, 1-4 93-118

[6] Feretti, L., Giovannini, G., Govoni, F., Murgia, M. 2012, A& A Review, 20, 54F

[7] Guidetti D., Laing R. A., Murgia M., et al. 2010, A& A, 514, A50

[8] Hatch N.A., Crawford C.S., et al. 2006, ESASP, 604, 689H

[9] Hudson D. S., Mittal R., Reiprich T. H., Nulsen P.E.J. et al. 2010, A& A, 513, A37, 44

[10] McNamara B. R. & O'Connell R. W. 1989, AJ, 98, 2018

[11] Molendi S., Pizzolato F. 2001, ApJ, 560, 194-200

[12] Rundnick L. & Blundell K. M. 2003, ApJ, 588, 143-154

[13] Sarazin C.L. 2002, Astroph. and Sp. Sc. Lib., 272, 1

[14] Sanders J. S., Fabian A. C., Hlavacek-Larrondo J., Russell H. R., et al. 2012, MNRAS, 444, 2, 1497-1517

[15] Sanders J. S., Fabian A. C., 2002, MNRAS, 331, 273

[16] Taylor G. B., Fabian A. C., Allen S. W., 2002, MNRAS, 334, 769

[17] Taylor G. B., Sanders J. S., Fabian A. C. Allen S. W., 2006, MNRAS, 365, 705

[18] Taylor G. B., Fabian A. C., Gentile G., Allen S. W., et al. 2007, MNRAS, 382 1, 67-72

[19] Vacca V., Murgia M., Govoni F., et al. 2010, A&A, 514, 71

[20] VLA OSS 2015A: Chromatic Aberation (Bandwidth Smearing), 2014, Retrived October 20, 2014 from https://science.nrao.edu/facilities/vla/docs/manuals/oss/performance/fov/bw-smearing

[21] VLA OSS 2015B: Time-Averaing Loss, 2014, Retrived October 20, 2014 from https://science.nrao.edu/facilities/vla/docs/manuals/oss/performance/fov/t-av-loss